INTERNATIONAL JOURNAL FOR NUMERICAL METHODS IN FLUIDS, VOL. 15, 1119–1141 (1992)

APPLICATIONS OF BOUNDARY INTEGRAL EQUATION METHODS FOR TWO-DIMENSIONAL NON-LINEAR WATER WAVE PROBLEMS

PHILIP L.-F. LIU AND H.-W. HSU

School of Civil and Environmental Engineering, Cornell University, Ithaca, NY 14853, U.S.A.

AND

MENG H. LEAN

Xerox Corporation, Webster Research Center, Mechanical Engineering Sciences Laboratory, North Tarrytown, NY 10591, U.S.A.

SUMMARY

On the basis of the integral equation approach, numerical algorithms for solving non-linear water wave problem are presented. The free surface flow is assumed to be irrotational. Two different Green functions are used in the integral equations. The non-linear free-surface boundary conditions are treated by a time-stepping Lagrangian technique. Several numerical examples are given, including permanent periodic waves, overturning progressive waves, breaking standing waves and sloshing problems.

KEY WORDS Integral equation Overturning progressive waves Breaking standing waves Sloshing

1. INTRODUCTION

The mathematical problem describing free surface flows is strongly non-linear because the free surface boundary conditions are not only quadratic in terms of the velocity field but also applied on the as yet undetermined free surface. In the past two decades many numerical models based on the integral equation approach have been developed to solve various free surface flow problems.[1, 2]

For two-dimensional flows two different approaches have been developed. The first approach is to convert the boundary value problem to an integral equation on the physical plane. The Green function used in this approach is usually the free space Green function (see Reference 3). Using this approach, Longuet-Higgins and Cokelet[4] calculated the overturning (breaking) of periodic deep water waves. Grilli *et al.*[5] have extended the approach to compute the breaking of periodic waves and a solitary wave in shallow water. Besides the wave-breaking problem, this approach has also been applied to other physical problems such as the sloshing problem,[6, 7] wave run-up on steep slopes[8, 9] and wave–structure interactions.[10]

The second approach employs the Cauchy integral theorem to derive the integral equation in terms of the complex potential function. Vinje and Brevig[11] presented this method with examples on periodic breaking waves. Many researchers have improved Vinje and Brevig's model by using more accurate numerical integration schemes (see e.g. References 12 and 13). This approach has

0271–2091/92/211119–23$16.50

Received March 1992

also been applied to other physical problems such as the wave-maker problem[14] and the free surface flow around a semi-finite body.[15]

Two primary issues concern every numerical free surface flow model based on the integral equation approach: (1) discretization of the boundary and the interpolation of variables over discretized boundaries; (2) the treatment of free surface boundary conditions. To improve the accuracy of the solutions, many researchers have used a higher-order interpolation function for both boundary discretization and numerical integrations. Unfortunately, the computational effort increases rapidly with higher-order elements.

There are many different schemes for treating the non-linear free surface boundary conditions. For example, the scheme developed by Kim *et al.*,[8] using the Crank–Nicolson method to move the free surface nodal points in specified directions, has been successfully applied to the wave run-up problem. Their method cannot be used to calculate the wave-breaking problem because the free surface nodes are not allowed to cross each other. The Eulerian–Lagrangian method introduced by Dold and Peregrine[12] is most suitable for calculating the wave-overturning profile. In their approach the free surface location and the associated velocity potential are expanded in Taylor series. The particle velocity, acceleration and other higher-order time derivatives are obtained by solving a series of integral equations.

In this paper we present a numerical model based on the integral equation approach. The model addresses two types of flows: periodic and non-periodic. For the periodic flows we employ two different Green functions: the conventional free space Green function and a periodic Green function. Using the periodic Green function, the integral equation is reduced to one integrating only over the free surface. The numerical efficiency of using these Green functions will be discussed in the numerical examples.

In the present model the boundary is divided into straightline elements and the physical variables are assumed to vary linearly over each element. The integral equations can then be integrated analytically (see e.g. Reference 16). The Eulerian–Lagrangian method is employed to track the free surface movement. It is necessary to compute the tangential derivatives of several physical variables such as the potential function and its normal derivatives. To accomplish these goals, the cubic B-spline interpolation scheme is used.

Several numerical examples are given herein. The accuracy of the numerical results is demonstrated by checking the conservation laws of mass and energy when possible.

2. GOVERNING EQUATION AND BOUNDARY CONDITIONS

In this paper we are interested in solving two-dimensional flows with a free surface. We assume that the fluid is inviscid and incompressible such that the velocity potential ϕ satisfies the Laplace equation

$$\nabla^2\phi = 0. \tag{1}$$

As shown in Figure 1, the computational domain Ω is bounded by a free surface Γ_f, a solid bottom Γ_b and two lateral boundaries Γ_l and Γ_r. Using the Cartesian co-ordinates (x, z), we can define the velocity components u and w in the forms

$$u = \frac{\partial\phi}{\partial x}, \qquad w = \frac{\partial\phi}{\partial z}. \tag{2}$$

Along the boundaries we can introduce a set of local co-ordinates (s, n), where $\mathbf{s}$ is the unit tangential vector and $\mathbf{n}$ is the unit outward normal. The velocity components u and w can also be written in terms of the tangential velocity component $\partial\phi/\partial s$ and the normal velocity component

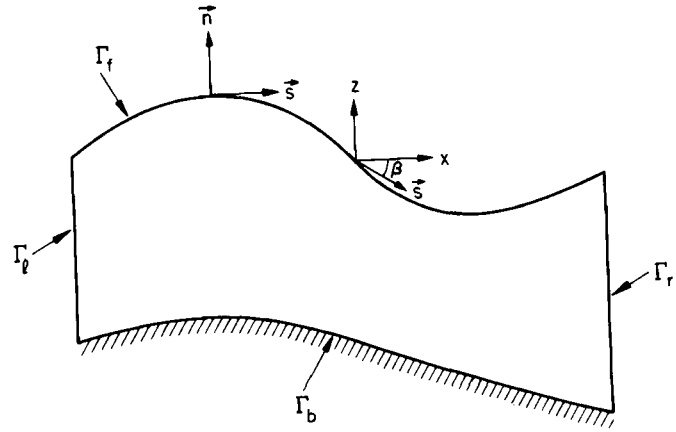

Figure 1. Definition sketch: computational domain, co-ordinates and free-surface angle

$\partial\phi/\partial n$, i.e.

$$u=\frac{\partial\phi}{\partial x}=\frac{\partial\phi}{\partial s}\cos\beta-\frac{\partial\phi}{\partial n}\sin\beta, \tag{3a}$$

$$w=\frac{\partial\phi}{\partial s}\sin\beta+\frac{\partial\phi}{\partial n}\cos\beta, \tag{3b}$$

where β is the angle between **s** and **x**.

On the bottom boundary Γ_b, the normal velocity component is zero, i.e.

$$\frac{\partial\phi}{\partial n}=0 \quad \text{on } \Gamma_b. \tag{4}$$

There are two boundary conditions on the free surface Γ_f. First we assume that the free surface is a material surface. Hence the fluid particles on the free surface will not leave the surface. Denoting the co-ordinates of fluid particles on the free surface as

$$x=\xi(t; x_o), \tag{5a}$$

$$z=\xi(t; z_o), \tag{5b}$$

where $x_o=\xi(0; x_o)$ and $z_o=\zeta(0; z_o)$, the kinematic boundary condition requires

$$\frac{d\xi}{dt}=u \quad \text{and} \quad \frac{d\zeta}{dt}=w \quad \text{on } \Gamma_f. \tag{6}$$

The second free surface boundary condition is derived from Bernoulli's equation, which can be written as

$$\frac{D\phi}{Dt}=-\frac{p}{\rho}-g\xi+\frac{1}{2}\left[\left(\frac{\partial\phi}{\partial x}\right)^2+\left(\frac{\partial\phi}{\partial z}\right)^2\right] \quad \text{on } \Gamma_f \tag{7}$$

where g is the gravitational acceleration, ρ is the density of the fluid and p is the pressure on the

free surface. In equation (7)

$$\frac{D}{Dt}=\frac{\partial}{\partial t}+\frac{\partial\phi}{\partial x}\frac{\partial}{\partial x}+\frac{\partial\phi}{\partial z}\frac{\partial}{\partial z} \tag{8}$$

represents the total time derivative, which calculates the time rate of change of a physical property following a fluid particle.

Two types of lateral boundary condition are employed in this paper. The first kind is the periodicity condition in which the flow is periodic in the x-direction. Hence

$$\phi|_{\Gamma_l}=\phi|_{\Gamma_r}, \qquad \left.\frac{\partial\phi}{\partial n}\right|_{\Gamma_l}=-\left.\frac{\partial\phi}{\partial n}\right|_{\Gamma_r}. \tag{9}$$

The second type of lateral boundary condition is to specify the normal fluxes on these boundaries, i.e. $\partial\phi/\partial n$ equals a known function of time.

3. INTEGRAL EQUATION

The boundary value problem described in the previous section can be converted into an integral equation integrating along the boundary $\Gamma(\Gamma_f\cup\Gamma_b\cup\Gamma_l\cup\Gamma_r)$. Using the Green second identity between the velocity potential ϕ and a Green function $G(\mathbf{x}, \mathbf{x}_o)$ which satisfies the Poisson equation

$$\nabla^2 G(\mathbf{x}, \mathbf{x}_o)=\delta(\mathbf{x}-\mathbf{x}_o), \tag{10}$$

where δ is the Dirac delta function, we obtain (see e.g. Reference 16)

$$\int_\Gamma\left(\phi\frac{\partial G}{\partial n}-G\frac{\partial\phi}{\partial n}\right)ds=\alpha\phi. \tag{11}$$

If the source point $\mathbf{x}_o$ is located on the boundary, α is the interior angle of the boundary at the source point. Equation (11) becomes an integral equation relating ϕ and $\partial\phi/\partial n$ along the boundary. On the other hand, if the source point is an interior point, α takes a value of 2π. Equation (11) can then be used to calculate the velocity potential at any interior point.

Different forms of Green function can be used in the integral equation (11). In this paper two kinds of Green function are used and corresponding solutions are compared. The first kind of Green function satisfies only the governing equation (10) without any boundary condition. Hence

$$G_f(\mathbf{x}, \mathbf{x}_o)=\ln r, \qquad r=|\mathbf{x}-\mathbf{x}_o|, \tag{12}$$

which is also called the free space Green function. The second kind of Green function is only suitable for periodic problems. Denoting λ as the wavelength in the x-direction of the periodicity, we can define the Green function as

$$G_p(\mathbf{x}, \mathbf{x}_o)=\sum_{j=\infty}^{\infty}(\ln r_j+\ln r'_j), \tag{13}$$

with

$$r_j=\{[x-(x_o+j\lambda)]^2+(z-z_o)^2\}^{1/2}, \tag{14a}$$

$$r'_j=\{[x-(x_o+j\lambda)]^2+(z+2h+z_o)^2\}^{1/2}, \tag{14b}$$

where h is the still water depth. The Green function given in equations (13) and (14) satisfies not only the governing equation (10) but also the periodic lateral boundary condition (9) as well as the

no-flux boundary condition along the bottom $z=-h$. The corresponding integral equation can be simplified to

$$\int_{\Gamma_f}\left(\phi\frac{\partial G_p}{\partial n}-G_p\frac{\partial\phi}{\partial n}\right)ds=\alpha\phi, \tag{15}$$

in which only the integration over the free surface is required. The advantages and disadvantages of using G_p will be discussed in the numerical examples.

4. NUMERICAL METHODS

To solve the integral equation (11) or (15), the boundary of the computational domain is divided into straight line segments. Within each segment the potential and its normal derivatives are assumed to vary linearly. Placing the source point $\mathbf{x}_0$ at each nodal point successively, we can integrate the integral equations analytically and obtain a system of linear algebraic equations for ϕ_j and $(\partial\phi/\partial n)_j$,

$$\sum_{j=1}^{N}R_{ij}\phi_j=\sum_{j=1}^{N}L_{ij}\left(\frac{\partial\phi}{\partial n}\right)_j,\quad i=1,2,\ldots,N, \tag{16}$$

in which N denotes the number of nodes on the boundary and ϕ_j and $(\partial\phi/\partial n)_j$ are the values of ϕ and $\partial\phi/\partial n$ at the jth node. In (16), R_{ij} and L_{ij} depend only on the geometry of the boundary and have analytical forms (see Reference 16).

To solve the system of linear algebraic equations, one must apply the boundary conditions. The implementation of the bottom and the non-periodic lateral boundary conditions is straightforward: $(\partial\phi/\partial n)$-values at these boundary nodes are substituted into the appropriate terms on the right-hand side of (16); ϕ-values will be obtained on these boundaries by solving (16). In the case of a periodic problem the boundary condition (9) is used to replace the unknown ϕ and $\partial\phi/\partial n$ on the downstream boundary by those on the upstream boundary.

The free surface boundary conditions (6) and (7) are non-linear not only because they are in quadratic form in terms of velocity but also because they are applied on the surface which is not known *a priori*. For two-dimensional problems several numerical schemes have been developed. For example, Kim *et al.*[8] used the Crank–Nicolson method to move the free surface nodal points in specified directions. They implemented the scheme successfully to study the run-up of a solitary wave. Dold and Peregrine[12] introduced the Taylor series expansion scheme which traces the fluid particle movements on the free surface. Therefore the scheme can be used to study steep waves and overturning waves.

In this paper we adopt Dold and Peregrine's approach with our own geometrical modelling technique. As indicated in (5), the free surface profile can be identified by tracking the position of fluid particles in time. Consider a fluid particle which moves from (ξ,ζ) at time t to a new position (ξ',ζ') at time $t+\Delta t$. If the time interval Δt is small, the new particle position (ξ',ζ') and the associated velocity potential ϕ' can be obtained by Taylor series expansions:

$$\xi'=\xi+\frac{d\xi}{dt}\Delta t+\frac{d^2\xi}{dt^2}\frac{(\Delta t)^2}{2}+O(\Delta t)^3, \tag{17a}$$

$$\zeta'=\zeta+\frac{d\zeta}{dt}\Delta t+\frac{d^2\zeta}{dt^2}\frac{(\Delta t)^2}{2}+O(\Delta t)^3, \tag{17b}$$

$$\phi'=\phi+\frac{D\phi}{Dt}\Delta t+\frac{D^2\phi}{Dt^2}\frac{(\Delta t)^2}{2}+O(\Delta t)^3, \tag{17c}$$

in which the right-hand-side terms are all evaluated at time t. If all the time derivatives of ξ, ζ and ϕ are known, the new particle location and the associated potential can be calculated to a desired accuracy. In this paper the numerical model includes only the second-order time derivatives.

From the free surface boundary condition (6) and the definition of the velocity field we can calculate the first time derivatives readily:

$$\frac{d\xi}{dt} = u = \frac{\partial \phi}{\partial s}\cos\beta - \frac{\partial \phi}{\partial n}\sin\beta \qquad \text{on } \Gamma_f, \tag{18a}$$

$$\frac{d\zeta}{dt} = w = \frac{\partial \phi}{\partial s}\sin\beta + \frac{\partial \phi}{\partial n}\cos\beta \qquad \text{on } \Gamma_f. \tag{18b}$$

The normal velocity component $\partial\phi/\partial n$ on the free surface is obtained directly from the solution of the boundary integral equation. One can complete the evaluation of (18) if the tangential derivative of ϕ, $\partial\phi/\partial s$, as well as the slope of the surface, β, can be estimated accurately. We use the B-spline scheme to model both ϕ and the free surface elevation, which will be described in the next section.

The total time derivative of ϕ on the free surface can be rewritten as

$$\frac{D\phi}{Dt} = -\frac{p}{\rho} - g\xi + \frac{1}{2}\left[\left(\frac{\partial \phi}{\partial s}\right)^2 + \left(\frac{\partial \phi}{\partial n}\right)^2\right] \qquad \text{on } \Gamma_f. \tag{18c}$$

Once again, the right-hand-side terms are known quantities; the pressure field on the free surface is usually a known quantity.

The second time derivatives of ξ, ζ and ϕ can be expressed as[5]

$$\frac{d^2\xi}{dt^2} = \frac{Du}{Dt} = \left(\frac{\partial \phi_t}{\partial s} + \frac{\partial \phi}{\partial s}\frac{\partial^2 \phi}{\partial s^2} + \frac{\partial \phi}{\partial n}\frac{\partial^2 \phi}{\partial n \partial s}\right)\cos\beta + \left(\frac{\partial \phi}{\partial n}\frac{\partial^2 \phi}{\partial s^2} - \frac{\partial \phi}{\partial s}\frac{\partial^2 \phi}{\partial n \partial s} - \frac{\partial \phi_t}{\partial n} - \frac{\partial \beta}{\partial s}(u^2 + w^2)\right)\sin\beta, \tag{19a}$$

$$\frac{d^2\zeta}{dt^2} = \frac{Dw}{Dt} = \left(\frac{\partial \phi_t}{\partial n} - \frac{\partial \phi}{\partial n}\frac{\partial^2 \phi}{\partial s^2} + \frac{\partial \phi}{\partial s}\frac{\partial^2 \phi}{\partial n \partial s} + \frac{\partial \beta}{\partial s}(u^2 + w^2)\right)\cos\beta + \left(\frac{\partial \phi_t}{\partial s} + \frac{\partial \phi}{\partial s}\frac{\partial^2 \phi}{\partial s^2} + \frac{\partial \phi}{\partial n}\frac{\partial^2 \phi}{\partial n \partial s}\right)\sin\beta, \tag{19b}$$

$$\frac{D^2\phi}{Dt^2} = -\frac{D}{Dt}\left(\frac{p}{\rho}\right) - g\frac{d\xi}{dt} + \frac{1}{2}u\frac{d^2\xi}{dt^2} + \frac{1}{2}w\frac{d^2\zeta}{dt^2}, \tag{19c}$$

in which

$$\phi_t = \frac{\partial \phi}{\partial t} = \frac{D\phi}{Dt} - (u^2 + w^2) \tag{20}$$

is the Eulerian time derivative of the potential. After the first-time-derivative problem is solved, ϕ_t becomes a known quantity on the free surface. However, the normal derivative of ϕ_t on the free surface is still needed to calculate the second time derivatives.

Because ϕ_t satisfies the Laplace equation, the integral equations for ϕ, (11) and (15), also govern ϕ_t. Using (20) as the boundary condition on the free surface and other appropriate boundary conditions, we can solve (11) or (15) to obtain $\partial\phi_t/\partial n$ on the free surface. We remark here that because the same set of integral equations is used for ϕ and ϕ_t, the coefficient matrices R_{ij} and L_{ij} in (16) remain the same. In other words, numerical integrations need to be performed only once.

5. GEOMETRICAL MODELLING

On the free surface boundary we need to calculate the shape of the free surface profile, β, and the tangential derivatives of the potential and its higher derivatives, such as $\partial\phi/\partial s$, $\partial^2\phi/\partial n\partial s$ and $\partial^2\phi/\partial s^2$ in (19). The cubic B-spline scheme is used for this purpose. Although the description of this curve-fitting scheme can be found in the literature (see e.g. Reference 17), we highlight the scheme here for completeness. The cubic B-spline scheme creates a curve which goes through every (N) data point and is C^2-continuous everywhere. To achieve this, a set of $(N+2)$ control points is introduced so that the straight line connection of these control points creates a convex hull confining the B-spline curve.[17] Denoting P_i $(i=1, 2, \ldots, N)$ as the physical variable attached to the ith node on the boundary and Q_i $(i=0, 1, \ldots, N+1)$ as the physical variable at the ith control point, the relationship between $\{P\}$ and $\{Q\}$ can be written as

$$\{P\}=[M]\ \{Q\}, \tag{21}$$

where

$$\{P\}=\begin{Bmatrix} P_1 \\ P_2 \\ \vdots \\ P_N \end{Bmatrix}, \qquad \{Q\}=\begin{Bmatrix} Q_0 \\ Q_1 \\ Q_2 \\ \vdots \\ Q_N \\ Q_{N+1} \end{Bmatrix}, \tag{22a}$$

$$[M]=\begin{bmatrix} 1 & 4 & 1 & 0 & 0 & 0 & . & . & . & 0 \\ 0 & 1 & 4 & 1 & 0 & 0 & . & . & . & 0 \\ . & . & . & . & . & . & . & . & . & . \\ . & . & . & . & . & . & . & . & . & . \\ 0 & 0 & 0 & 0 & 0 & 0 & 1 & 4 & 1 & 0 \\ 0 & 0 & 0 & 0 & 0 & 0 & 0 & 1 & 4 & 1 \end{bmatrix}. \tag{22b}$$

Note that $\{P\}$ is an $N\times 1$ vector, $\{Q\}$ is an $(N+2)\times 1$ vector and $[M]$ is an $N\times(N+2)$ tridiagonal matrix. Because the value of the physical variable is given at nodal points, i.e. $\{P\}$ is known, (21) can be used to determine the value of the physical variable at the control points $\{Q\}$ provided that two more conditions are introduced. For the periodic problem the periodic boundary conditions are used, i.e. the first and second derivatives of $\{P\}$ with respect to η are required to be periodic. In the non-periodic situation additional conditions are provided by calculating the slopes of the curve at end points based on a local four-point curve-fitting scheme.

Once $\{Q\}$ is determined, the variation of the physical variable between two adjacent nodal points can be found in terms of a single parameter η and four control points as[11]

$$P(\eta)=\tfrac{1}{6}(\eta^3, \eta^2, \eta, 1)\begin{bmatrix} -1 & 3 & -3 & 1 \\ 3 & -6 & 3 & 0 \\ -3 & 0 & 3 & 0 \\ 1 & 4 & 1 & 0 \end{bmatrix}\begin{Bmatrix} Q_{i-1} \\ Q_i \\ Q_{i+1} \\ Q_{i+2} \end{Bmatrix}, \tag{23}$$

in which $0\le\eta\le 1$ with $P(0)=P_i$ and $P(1)=P_{i+1}$. When the co-ordinates of the free surface are used in (21), equation (23) provides the transformation between the physical space (ξ, ζ) and the

parametric space η. Denoting s as the measure of the arc length along the free surface, the transformation Jacobian J can be defined as

$$J=\frac{d\eta}{ds}=\left[\left(\frac{dx}{\partial\eta}\right)^2+\left(\frac{\partial z}{\partial\eta}\right)^2\right]^{-1/2}, \tag{24}$$

in which $\partial x/\partial\eta$ and $\partial z/\partial\eta$ can be readily obtained from (23), i.e.

$$\frac{\partial x}{\partial\eta}=\frac{1}{6}(\eta^2,\eta,1)\begin{bmatrix}-3 & 9 & -9 & 3\\ 6 & -12 & 6 & 0\\ -3 & 0 & 3 & 0\end{bmatrix}\begin{Bmatrix}Q_{i-1}\\ Q_i\\ Q_{i+1}\\ Q_{i+2}\end{Bmatrix}, \tag{25}$$

and the form for $\partial z/\partial\eta$ is exactly the same; the values of the control points are of course different. The second derivative $\delta^2x/\partial\eta^2$ can also be readily expressed as

$$\frac{\partial^2x}{\partial\eta^2}=\frac{1}{6}(\eta,1)\begin{bmatrix}-6 & 18 & -18 & 6\\ 6 & -12 & 6 & 0\end{bmatrix}\begin{Bmatrix}Q_{i-1}\\ Q_i\\ Q_{i+1}\\ Q_{i+2}\end{Bmatrix}, \tag{26}$$

Since the slope of the free surface profile is defined as (see Figure 1)

$$\beta=\tan^{-1}\left(\frac{\partial x/\partial s}{\partial z/\partial s}\right)=\tan^{-1}\left(\frac{\partial x/\partial\eta}{\partial z/\partial\eta}\right), \tag{27}$$

the derivative of β with respect to the arc length along the free surface can be written as

$$\frac{\partial\beta}{\partial s}=\frac{(\partial^2x/\partial\eta^2)\partial z/\partial\eta-(\partial^2z/\partial\eta^2)\partial x/\partial\eta}{(\partial x/\partial\eta)^2+(\partial z/\partial\eta)^2}J, \tag{28}$$

which can be calculated by using (25) and (26). The above equation is needed in evaluating (19a) and (19b).

The cubic B-spline scheme is also used to determine $\partial\phi/\partial s$, $\partial^2\phi/\partial n\partial s$ and $\partial^2\phi/\partial s^2$. For $\partial\phi/\partial s$ the control points are first determined based on the ϕ-values at each free surface nodal points. Once the vector $\{Q\}$, is found, the tangential derivative of ϕ can be written as

$$\frac{\partial\phi}{\partial s}=J\frac{\partial\phi}{\partial\eta}=\frac{1}{6}J(\eta^2,\eta,1)\begin{bmatrix}-3 & 9 & -9 & 3\\ 6 & -12 & 6 & 0\\ -3 & 0 & 3 & 0\end{bmatrix}\begin{Bmatrix}Q_{i-1}\\ Q_i\\ Q_{i+1}\\ Q_{i+2}\end{Bmatrix}. \tag{29}$$

The same formula can be used for $\partial^2\phi/\partial n\partial s$. except that the control points $\{Q\}$ are determined from the nodal point values of $\partial\phi/\partial n$. The second derivative of ϕ with respect to s can be written as

$$\frac{\partial^2\phi}{\partial s^2}=J^2\frac{\partial^2\phi}{\partial\eta^2}-J^4\frac{\partial\phi}{\partial\eta}\left(\frac{\partial^2x}{\partial\eta^2}\frac{\partial x}{\partial\eta}+\frac{\partial^2z}{\partial\eta^2}\frac{\partial z}{\partial\eta}\right). \tag{30}$$

The formula for the second derivative of ϕ with respect to η is the same as (26) with $\{Q\}$ being determined from the vector $\{\phi\}$ on the free surface.

6. NUMERICAL EXAMPLES

On the basis of the algorithm discussed herein, computer programmes have been written in Fortran. Several numerical examples are discussed in this section.

6.1. Permanent periodic waves

To verify the numerical scheme, we first calculate the propagation of a train of permanent periodic waves and compare the numerical results with the analytical expressions obtained by the streamfunction wave theory.[18, 19] The wave properties employed in the computations are as follows (see p. 392 of Reference 19): wavelength $\lambda = 26{\cdot}43$ m, wave height $H = 2{\cdot}10$ m, water depth $h = 12{\cdot}49$ m and wave period $T = 4$ s. The wave slope $\pi H/\lambda$ is approximately 0·25. The wave train is non-linear but stable.

Both the free space Green function (12) and the periodic Green function (13) are used in the numerical experiments. When the free space Green function is employed, the boundary consists of the free surface, two lateral vertical boundaries and the horizontal bottom. The length of the computational domain is one wavelength. Several different combinations of element sizes and time step sizes have been tried. The numerical solutions shown in Figure 2 are obtained using 100 elements on the boundary (40 elements on the free surface and 20 elements each on the lateral and bottom boundaries). The time step size is 0·02 s, which is 1/200th of one wave period. Figure 2 shows the comparison between numerical results and streamfunction solutions over 12 wave periods. The agreement is very good.

To further ensure the accuracy of the numerical solutions, the conservation of mass and energy is examined. First, integrating the free surface elevation over a wavelength should result in a zero

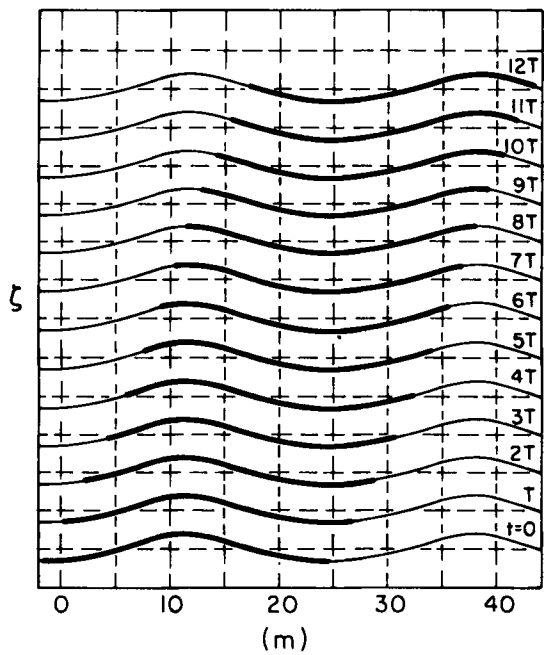

Figure 2. Evolution of a permanent wave train over 12 wave periods: ——, streamfunction solutions; ——, present numerical solutions

quantity. However, owing to numerical inaccuracy, we can define an error term as

$$\varepsilon_m = \frac{1}{H\lambda}\int_{\Gamma_f} \zeta \, dx, \tag{31}$$

where H is the initial wave height and λ is the wavelength.

The kinetic energy and the potential energy of the periodic waves can be calculated from

$$E_k = \frac{\rho}{2\lambda}\int_{\Gamma_f} \phi \frac{\partial \phi}{\partial n} \, ds, \tag{32}$$

$$E_p = \frac{\rho g}{2\lambda}\int_{\Gamma_f} \zeta^2 \, dx, \tag{33}$$

in which ρ is the density and g is gravitational acceleration. The total energy is the sum of kinetic and potential energy. Thus $E_T = E_k + E_p$. The relative error is defined as

$$\varepsilon_e = \frac{|E_T - E_T^0|}{E_T^0}, \tag{34}$$

where E_T^0 is the total energy calculated from initial conditions.

In Figures 3(a)–3(d) numerical results of the free surface profile at the end of the 12th wave period are compared with streamfunction solutions. In these computations 100 elements are used to represent the boundary. However, different time step sizes are employed. Numerical results obtained using larger time step sizes $\Delta t = T/100$ and $T/50$ show that the phase speeds are slightly larger than those predicted by the streamfunction theory. In the same set of figures the errors for the conservation of mass and energy are also plotted for each different time step size used. It is quite obvious that both errors decrease when Δt decreases. Specifically, when Δt is smaller than $T/200$, both errors are smaller than 0·2% during the first 12 wave periods. For the time step size $\Delta t = 0{\cdot}08$, s $= T/50$ a significant amount of error in total energy is accumulated even though the

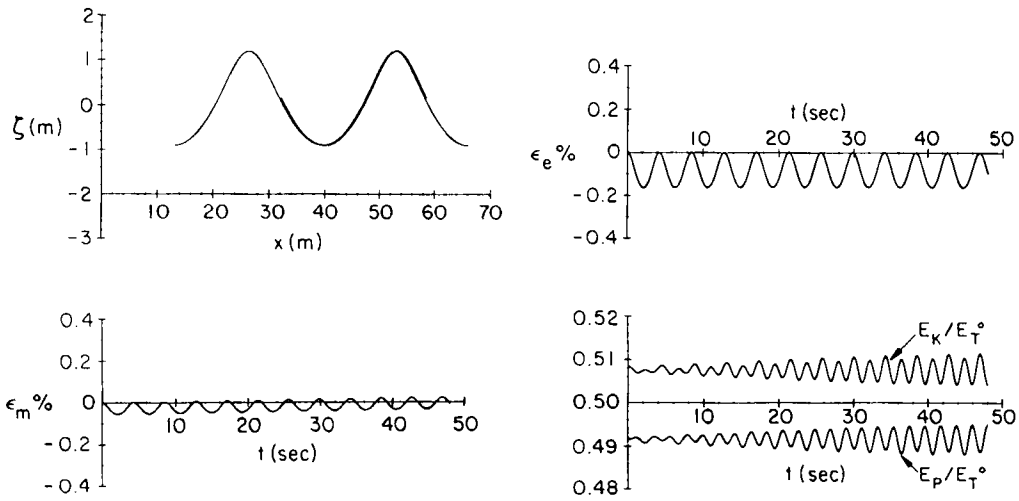

Figure 3(a). Numerical solutions for a permanent wave train. (1) Free surface profile at the end of the 12th wave period; ——, streamfunction solution; ——, present solution. (2) Time history of numerical error in mass conservation. (3) Time history of numerical error in energy conservation. (4) Time history of normalized kinetic and potential energy. To obtain the numerical solutions, 100 elements have been used and the time step size is 0·01 s

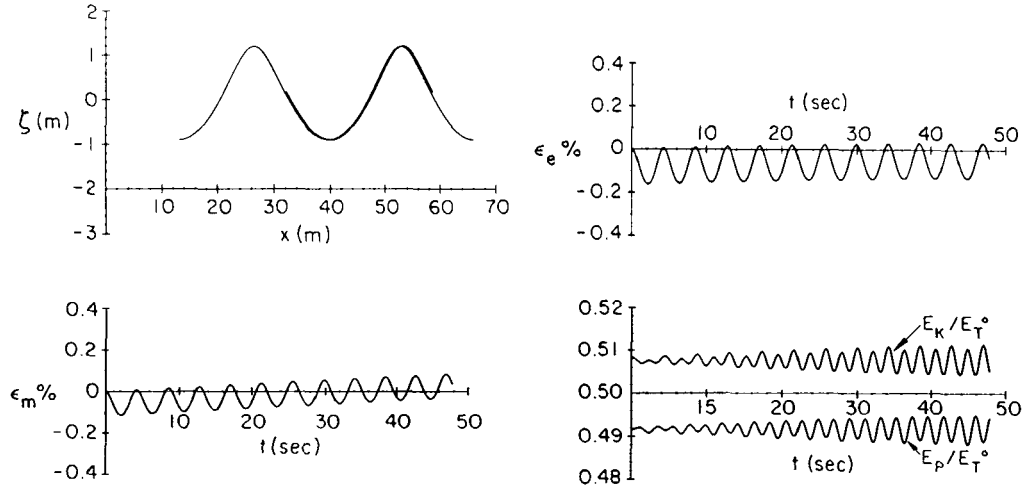

Figure 3(b). See caption of Figure 3(a). The time step size is 0·02 s

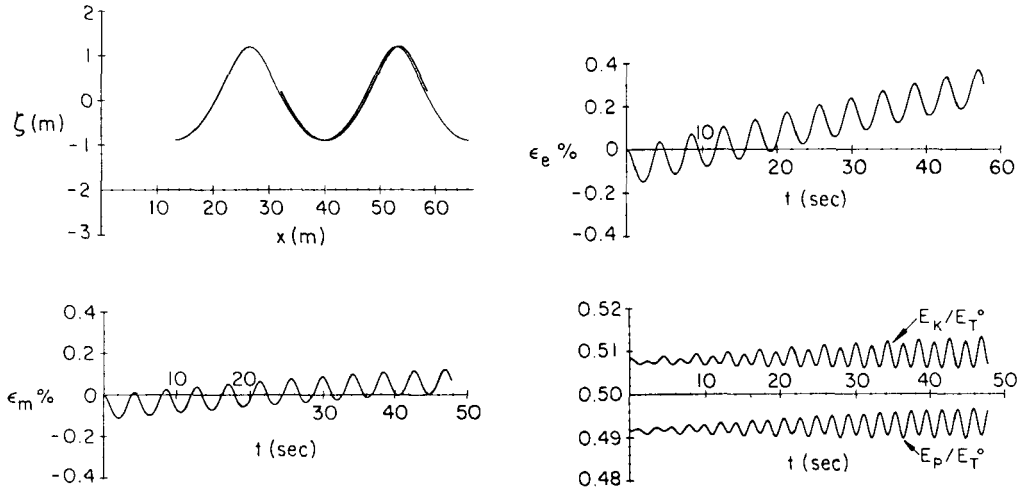

Figure 3(c) See caption of Figure 3(a). The time step size is 0·04 s

mass conservation is generally satisfied. The algorithm breaks down soon after $t = 11T$. Numerical experiments have also been performed to examine the effects of element size. In Figure 4 numerical solutions are shown for the case where only 50 elements are distributed along the boundary (20 elements on the free surface and 10 elements each on the other three boundaries). The time step size is $\Delta t = 0{\cdot}01$ s $= T/400$. The effects of increasing element sizes are equivalent to those of increasing time step sizes, i.e. numerical solutions have a faster phase speed and the relative errors in mass and energy conservation also increase.

In all the numerical results shown, the second time derivatives are calculated in the numerical scheme for tracking the free surface particles. One can, however, achieve similar accurate numerical results without including the second time derivatives by using very small time step sizes

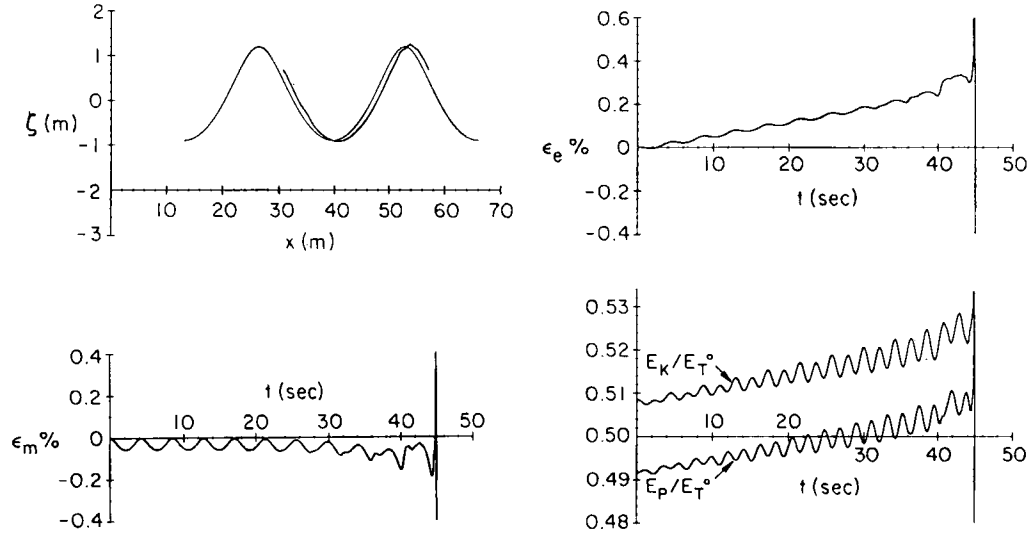

Figure 3(d) See caption of Figure 3(a). The time step size is 0·08 s

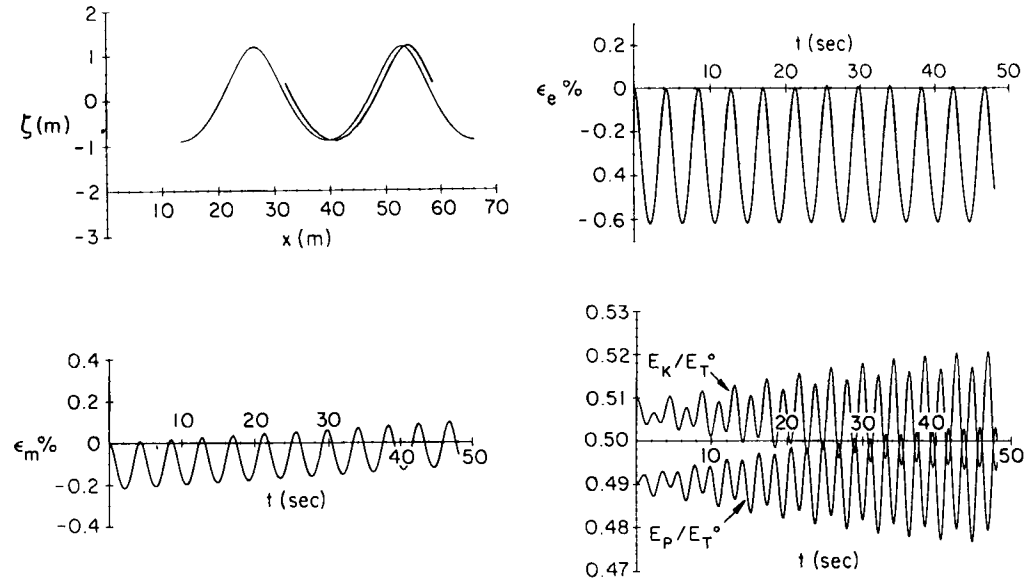

Figure 4. See caption of Figure 3(a). In this set of computations 50 elements have been used and the time step size is 0·01 s

(see equation (17)). A typical set of results is shown in Figure 5, in which 100 elements are used and the time step size is $\Delta t = 0{\cdot}0005$ s. Without calculating the second time derivatives, we save some computing time. However, this is not enough to offset the increase in computing time, because a much smaller time step size is required. Moreover, the errors in total energy are still 10 times higher than those obtained with the second time derivatives.

Numerical solutions are also obtained by using the periodic Green function (13). In this approach only the free surface is discretized. However, a large number of terms must be used in

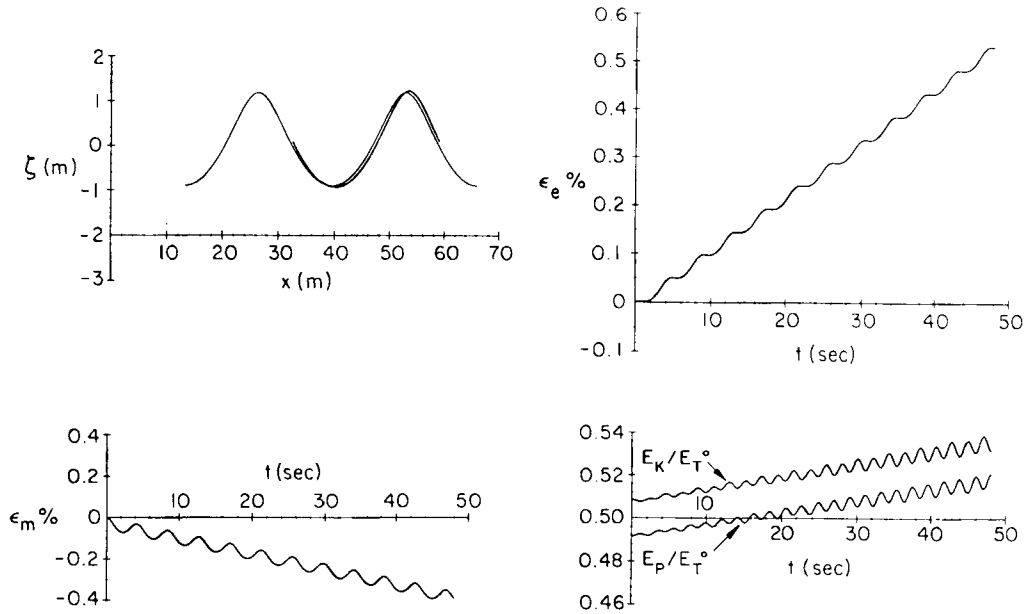

Figure 5. See caption of Figure 3(a). In this set of computations, only the first time derivatives were used in tracking the free surface movements; 100 elements were used and the time step size was 0·0005 s

Table I. FLOPS required for using the periodic Green function and the free-space Green function

	Periodic Green function	Free-space Green function
Integrations	$65\ (\alpha n)\ (2\alpha mn)$	$65n^2$
Decomposition	$\frac{2}{3}(\alpha n)^3$	$\frac{2}{3}n^3$
Backward substitution	$(\alpha n)^2$	n^2
Total	$(130\,m+1)\alpha^2n^2+\frac{2}{3}\alpha^3n^3$	$66n^2+\frac{2}{3}n^3$

n: total number of elements
αn: number of elements on the free surface
m: number of terms used in the periodic Green function

the periodic Green function. Because of the slow rate of convergence of the logarithmic functions for the permanent waves studied in this section, 81 terms are necessary to obtain the same accurate solutions as those obtained from the free space Green function approach (see Figure 6). In Table I we estimate the FLOPS required for these two approaches. It is quite clear that the approach using the periodic Green function becomes more efficient only if the number of elements is large. For the two-dimensional problem studied here ($n=100$, $m=81$, $\alpha n=40$), the total FLOPS are $1{\cdot}7\times10^7$ for using the periodic Green function and $1{\cdot}3\times10^6$ for using the free space Green function. The approach using the free space Green function is about eight times faster than that using the periodic Green function. The periodic Green function approach could become more efficient for three-dimensional problems, in which a much larger number of elements are required and the ratio of the number of free surface elements to the total number of

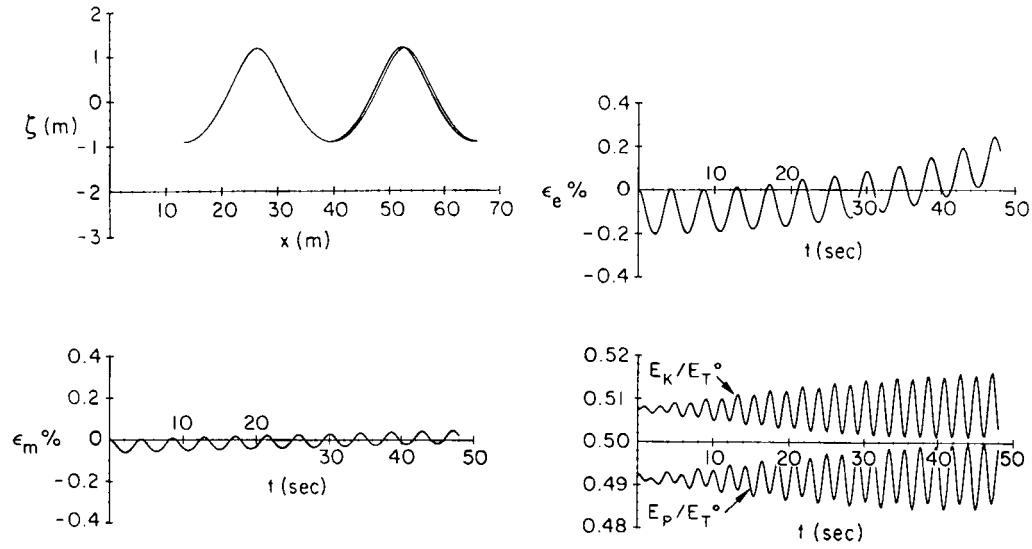

Figure 6. See caption of Figure 3(a). The periodic Green function was used in the computations; 81 terms were included; the free surface was divided into 40 elements and the time step size was 0·02 s

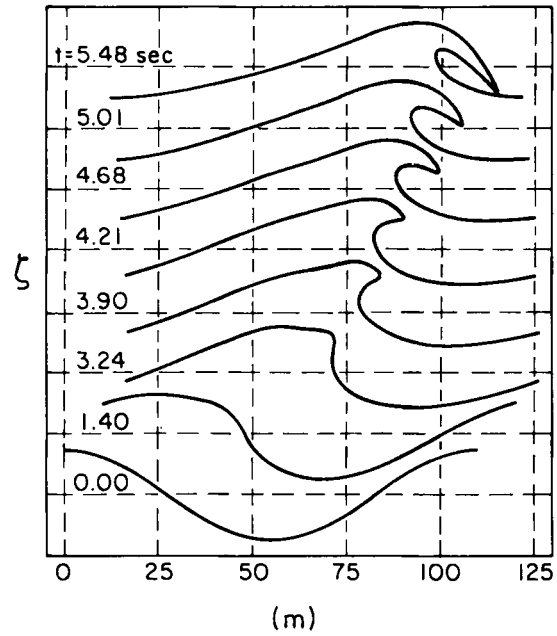

Figure 7. Evolution and overturning of a finite amplitude periodic wave train

elements (α) is smaller. Moreover, for three-dimensional problems the Green function $1/r$ should converge much faster than $\ln r$. Hence, if we use the following data for a three-dimensional problem—$n=600$, $\alpha=0{\cdot}16$, $m=21$—the total FLOPS are $2{\cdot}6\times10^7$ for using the periodic Green function and $1{\cdot}8\times10^8$ for using the free space Green function.

6.2. Overturning waves

The numerical schemes developed for permanent waves are extended to simulate overturning waves. The initial conditions used are sinusoidal waves with a rather large wave amplitude. The wave parameters are: wave height $H = 20{\cdot}0$ m, wavelength $\lambda = 110{\cdot}0$ m, water depth $h = 60{\cdot}0$ m and wave period $T = 8{\cdot}4$ s. The wave slope $\pi H/\lambda$ is approximately 0·57 and is over the stability limit.

In the numerical experiments several combinations of different element sizes are tested. For instance, the numerical results shown in Figure 7 were obtained with 140 elements on the boundary (80 elements on the free surface and 20 elements each on the other boundaries). In this figure the evolution of the unstable waves is demonstrated. The free surface develops a vertical front at $= 3{\cdot}00$ s. After that time the overturning process begins. The time step size is actually defined to be the maximum value that allows all surface nodes to travel less than or equal to half of the minimum distance between two adjacent nodes.

The computation eventually terminates when the tip of the water jet reaches the lower part of the free surface. An automatic regridding routine has been employed to obtain the results shown in Figure 7. Without the regridding routine the numerical scheme breaks down before the jet reaches the free surface. The reason for the breakdown can be seen in Figure 8, in which a time sequence of velocity vectors in the vicinity of the tip of the water jet is plotted. Two important features are revealed: (1) element size becomes very small near the tip, which results in an ill-conditioned system of equations; (2) the velocity vectors cross each other near the tip. A regridding algorithm is necessary and is implemented in the following manner. The largest and smallest elements on the free surface are identified at each time step. When the ratio between the lengths of the maximum element and the smallest element is greater than 18, the nodal points between these extreme elements are shifted by a small amount such that the length ratio becomes smaller than 18. This simple regridding scheme shows that the condition number of the matrix equation does not increase drastically. This regridding scheme works very well for overturning problems. It has not been proven for general problems.

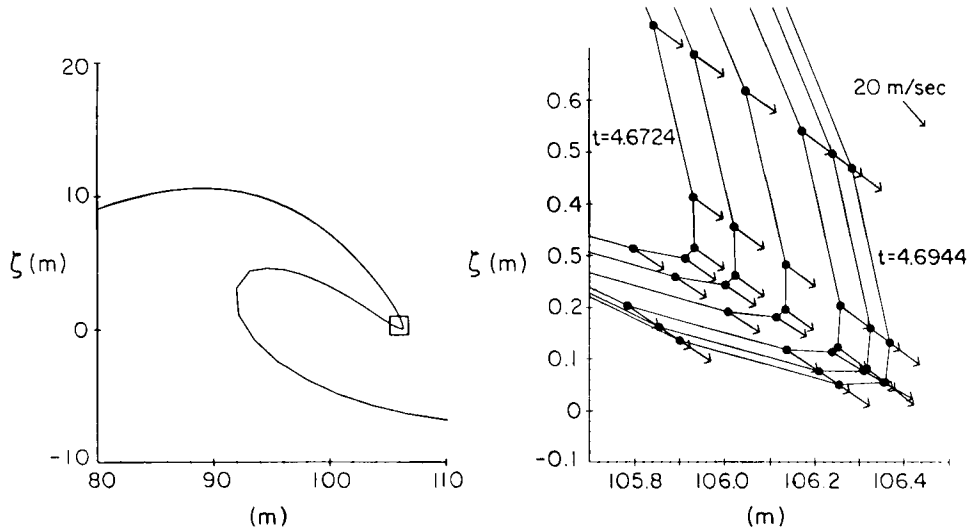

Figure 8. Numerical solutions in the neighbourhood of the time of an overturning wave

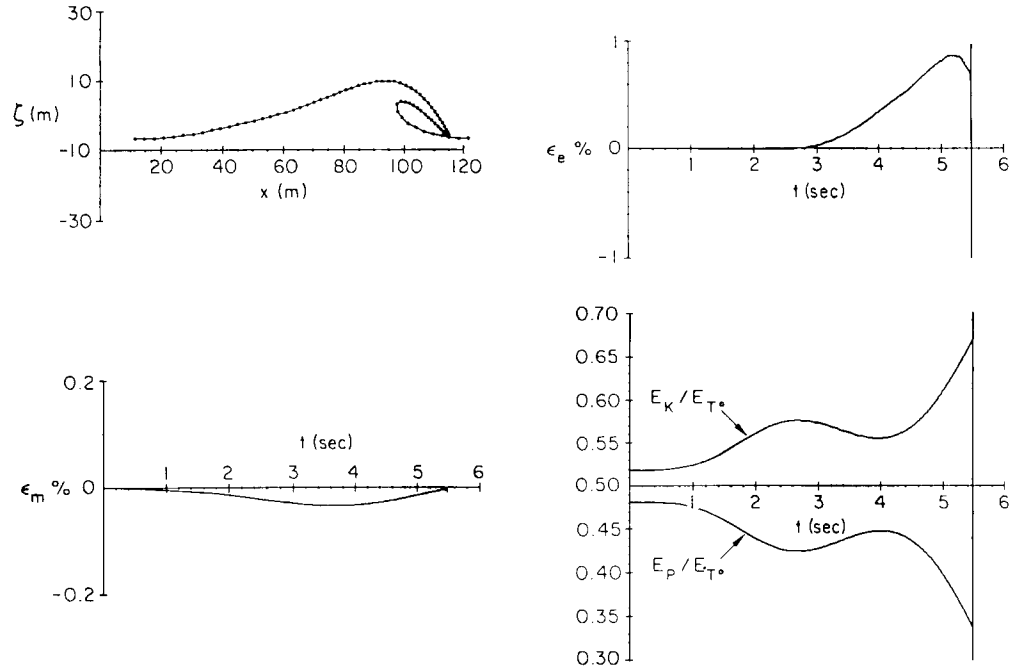

Figure 9(a). Numerical solutions for a periodic overturning wave train. (1) Free surface profile at $t = 5{\cdot}48$ s. (2) Time history of numerical error in mass conservation. (3) Time history of numerical error in energy conservation. (4) Time historty of normalized kinetic energy and potential energy. In the numerical computations the boundary is divided into 140 elements

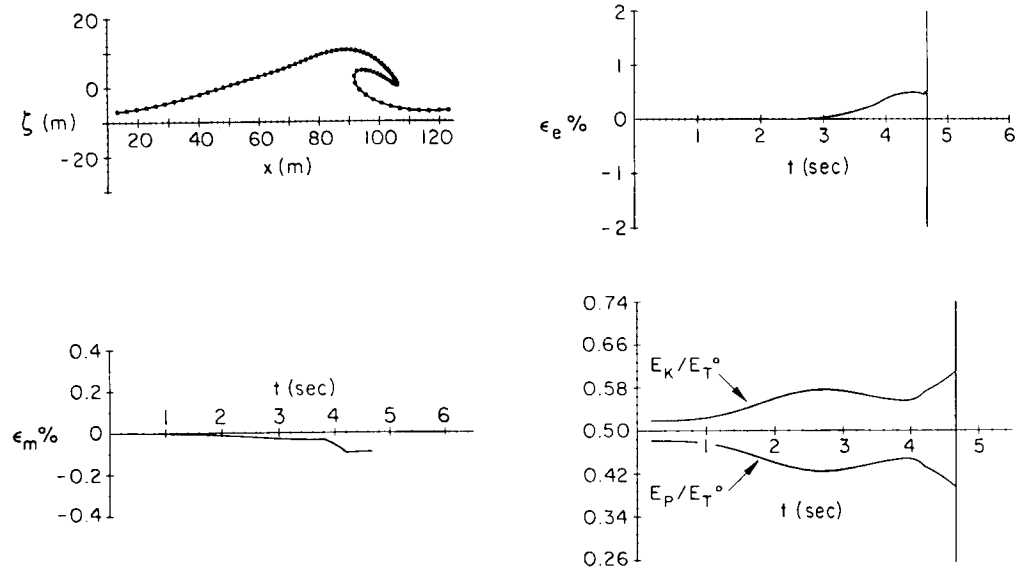

Figure 9(b). As for Figure 9(a) but without regridding

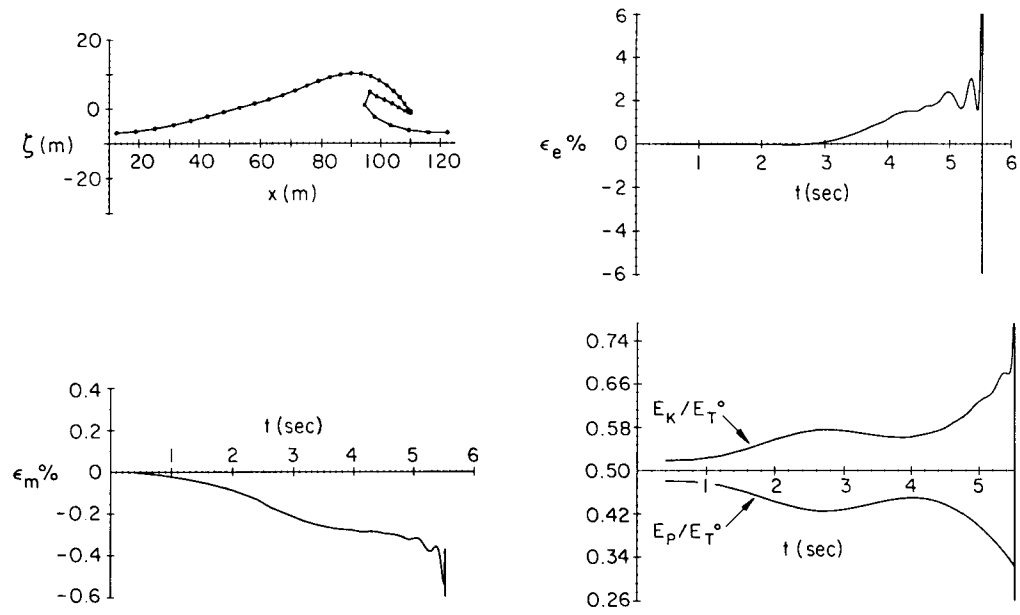

Figure 9(c). See caption of Figure 9(a). The boundary is divided into 100 elements

In Figures 9(a)–9(c) three sets of numerical results are presented to demonstrate the conservation properties of the numerical scheme. Numerical results shown in Figure 9(a) are obtained by using 140 elements with 80 elements on the free surface and 20 elements each on the other three boundaries. The regridding scheme is used in this case. Figure 9(b) show numerical solutions obtained by using the same discretization but without the regridding scheme. In Figure 9(c) 100 elements are used with 40 elements on the free surface and 20 elements each on the other three boundaries. In all three cases numerical errors are presented in terms of energy conservation and mass conservation. It is interesting to note that the total energy is almost perfectly conserved up to $t=3{\cdot}0$ s, at which time the free surface becomes vertical. The mass conservation is satisfied within 0·2% up to the time when the system breaks down. Numerical solutions are also obtained using the periodic Green function. When more than 81 terms are used in the periodic Green function, the numerical solutions obtained from the two different Green functions are almost identical.

6.3. Sloshing problem

The third example concerns sloshing in a rectangular basin. The depth of the basin is $h=0{\cdot}6$ m and the width is $W=0{\cdot}9$ m. The basin is forced to oscillate horizontally. The response of the free surface movement is sought. The natural frequencies of the sloshing modes can be estimated as

$$\omega_n=\left[g\frac{2\pi}{L_n}\tanh\left(\frac{2\pi h}{L_n}\right)\right]^{1/2}, \tag{35}$$

where $L_n=2W/(2n+1)$ with an integer n. The natural frequency of the first mode ($n=0$) for this basin is

$$\omega_0=5{\cdot}761\ \mathrm{s}^{-1}.$$

If the forcing frequency is near the natural frequency, the free surface oscillation can be resonated. Two sets of numerical solutions are presented here. In the first problem the forcing frequency is $\omega_f = 5{\cdot}5\ s^{-1}$, while the second problem has a forcing frequency $\omega_f = 5{\cdot}0\ s^{-1}$. The first problem observes the resonance phenomenon.

To obtain the numerical solutions, the lateral boundary conditions are specified as

$$X(t) = x_0 \cos \omega_f t \qquad \text{on } \Gamma_l \text{ and } \Gamma_r, \tag{36}$$

$$\frac{\partial \phi}{\partial n} = \pm \omega_f x_0 \sin \omega_f t \qquad \text{on } \Gamma_l \text{ and } \Gamma_r, \tag{37}$$

where x_0 is the amplitude of the basin oscillation. In the first problem $\omega_f x_0 = 0{\cdot}02\ m\,s^{-1}$, while $\omega_f x_0 = 0{\cdot}06\ m\,s^{-1}$ for the second problem. The treatment of corner points, the intersection point of the free surface and the vertical wall, is described here. We assume that the fluid particle occupying the corner will be a corner point forever. Hence the velocity vector at the corner point can be obtained from the information associated with the vertical wall (lateral boundary), i.e. the velocity component normal to the vertical is given in the boundary condition and the tangential velocity can be determined from the distribution of the potential function along the vertical wall. This approach has been generalized for an inclined side wall and is more accurate than other existing aproximated treatments (see e.g. Reference 7).

In both computations the boundary is divided into 100 elements; (40 elements on the surface and 20 elements each on the lateral boundaries and the bottom boundary). The time step size is chosen to be 0·004 s.

In Figure 10 the time history of the free surface displacement at the left corner point is plotted for the first problem. Since the forcing frequency is close to the natural frequency, the wave amplitude grows almost linearly in time. The corresponding time histories of the normalized potential energy and the normalized total energy are presented in Figure 11. The normalization factor is $\rho g W x_0$. Because the sloshing motion is the first-mode ($n = 0$) oscillations, the free surface profile becomes horizontal periodically. Hence the potential energy also becomes zero periodically. It is interesting to observe that the total energy increases, but not monotonically, in time.

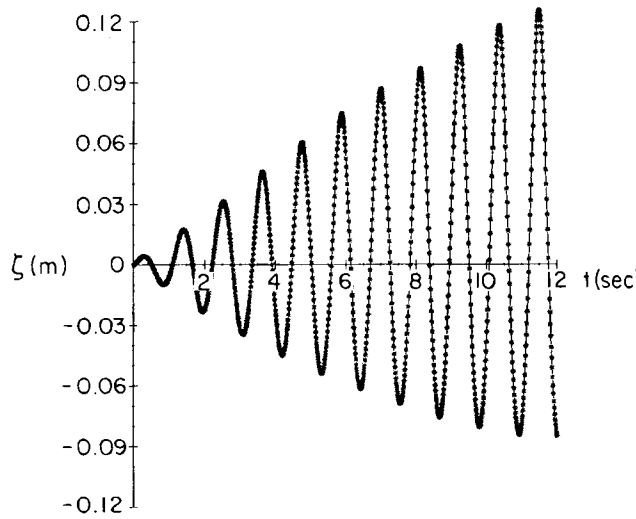

Figure 10. Free surface displacement at the left corner of the oscillating tank

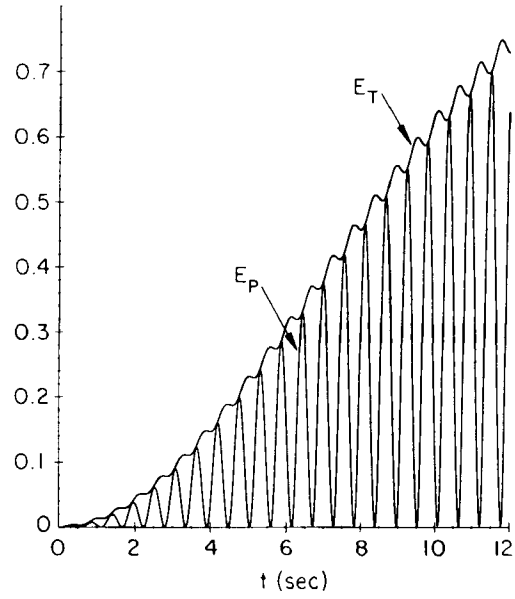

Figure 11. Normalized potential energy and total energy for the sloshing resonant mode

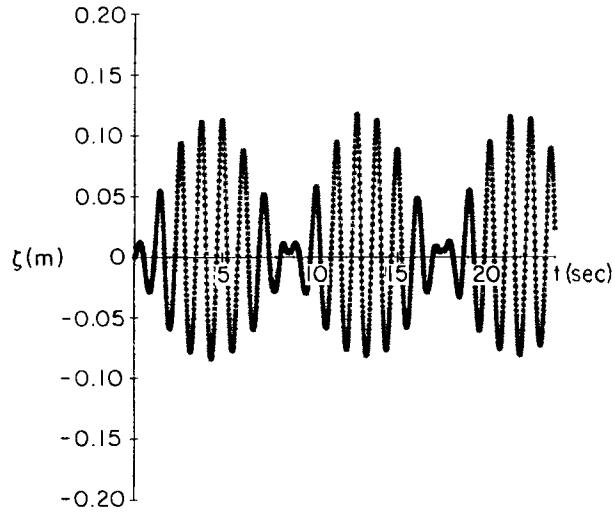

Figure 12. Free surface displacement at the left corner of the tank for the non-resonance case

For the second problem the forcing frequency is $\omega_f = 5.0\ s^{-1}$, which is quite different from the natural frequency of the basin, $\omega_o = 5{\cdot}761\ s^{-1}$. Because of the frequency difference, a 'surf beat' phenomenon is observed in the basin. In Figure 12 the time history of the free surface displacement at the left corner is shown. The wave period of the 'beats' (or 'groups') can be estimated as $T = 2\pi/(\omega_o - \omega_f) = 9{\cdot}03$ s. The normalized total energy and the normalized potential energy are

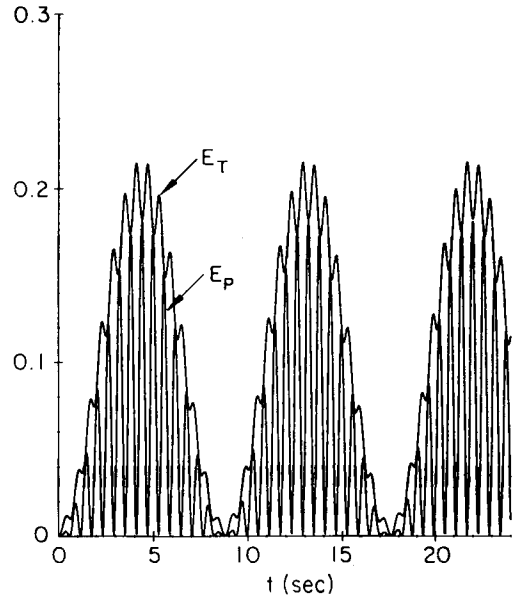

Figure 13. Normalized potential and total energy for the non-resonance sloshing mode

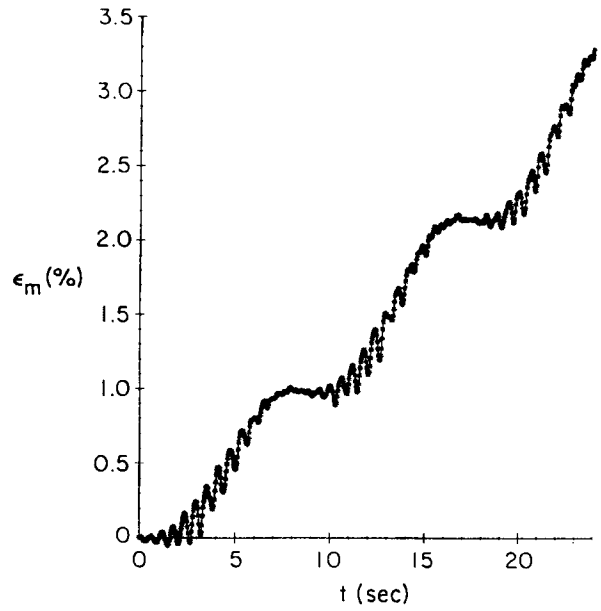

Figure 14. Time history of numerical error in mass conservation for the non-resonance sloshing mode

plotted in Figure 13. To check the conservation of mass, the dimensionless mean water level is shown in Figure 14. The stroke (0·012 m) has been used as the normalization factor, which is roughly 10 times the maximum wave amplitude. The maximum error is less than 3·5% after more than 5000 time step computations.

6.4. Highest standing waves

The last example calculates the free surface profile for highest standing waves. Taylor[20] performed laboratory experiments and showed a highest wave crest of nearly 90°. He confirmed Peney and Price's[21] theoretical prediction that the maximum wave height/wavelength ratio is 0·218. Using a higher-order theory, Schwartz and Whitney[22] showed that this ratio should be 0·208.

In Taylor's experiments the water depth is 15·5 cm and the length of the tank is 32·9 cm. A hinged type of wave-maker was installed at both ends of the tank. The depth of the hinge was 10 cm and the length of the wave-maker is 22·6 cm. The natural frequency of the wave tank can be calculated from (35) with $L=32{\cdot}9$ cm and $h=15{\cdot}5$ cm, which results in $T=13{\cdot}653$ s. The laboratory experiments satisfy the deep water condition.

In the present computations three wave depths are used, $h=5$, 10 and 15·5 cm. The length of the tank is the same as that of Taylor's experiment. Two piston-type wave-makers are used as the boundary conditions:

$$\frac{\partial \phi}{\partial n}=\omega x_0 \sin(\omega t) \quad \text{on } \Gamma_l \text{ and } \Gamma_r. \tag{38}$$

The wave-makers stop moving after four wave periods. The strokes are varied such that standing waves remain in the basin after the wave-makers are stopped. The maximum wave height is determined when the acceleration of the fluid particle at the crest becomes larger than the gravitational acceleration. In the present computations the stroke is 1% of the wavelength. The boundary is divided into 120 elements (50 elements on the free surface, 20 elements each on the lateral boundaries and 30 elements on the bottom boundary). The time step size is 0·0005 s.

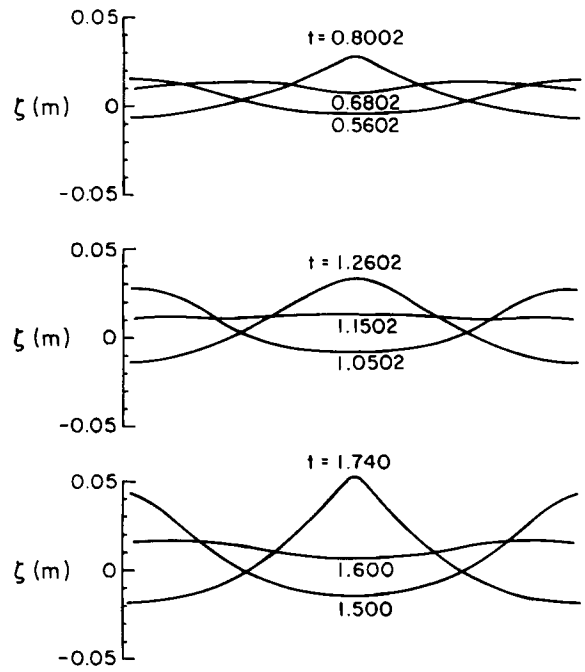

Figure 15. Evolution of free surface displacements of a standing wave; the water depth is 15·5 cm

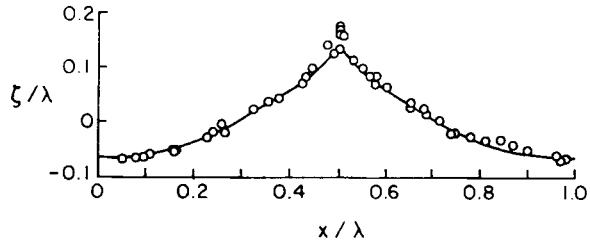

Figure 16. Comparison between numerical results (——) and Taylor's experimental data (○○○)

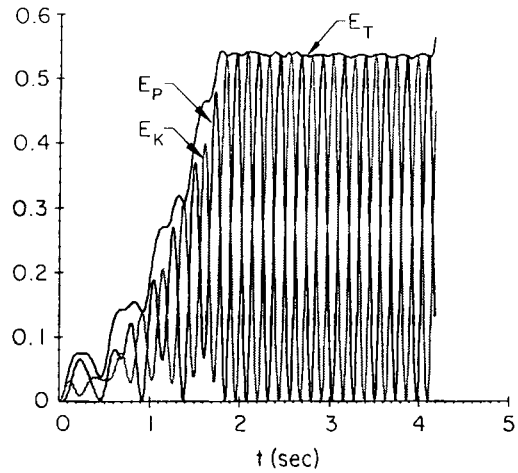

Figure 17. Time history of energy components in a standing wave; the wave-maker was stopped at the end of the fourth period

In Figure 15 the evolution of free surface displacements is displayed for the case where $h = 15{\cdot}5$ cm. Because of the resonance, the amplitudes grow in time. The maximum wave height is reached at $t = 1{\cdot}74$ s. The comparison between the numerical solutions and Taylor's experimental data is given in Figure 16. The agreement is reasonable. The wave steepness H/λ is about 0·195, which is lower than predicted by theory. The minimum angle at the crest is almost 90°. In Figure 17 the time history of energy components is shown. The total energy remains constant after the wave-makers stop moving.

For the shallower water case, $h = 5$ cm, the wave steepness at the maximum wave height is smaller, $H/\lambda = 0{\cdot}152$. However, the minimum surface angle at the crest remains as 90°.

7. CONCLUDING REMARKS

A numerical algorithm has been developed for tracking the free surface movement in two dimensions. The algorithm is very robust and is used to produce solutions for highly non-linear problems such as overturning waves and highest standing waves. The accuracy of the solutions has been examined by checking the conservation of mass and energy.

The periodic Green function introduced in the paper does not show any advantage in terms of computational efficiency over the free surface Green function. However, it has been demonstrated

that for a three-dimensional problem where the ratio of the number of free surface elements to the total number of boundary elements is small the periodic Green function approach can gain significant efficiency.

ACKNOWLEDGEMENT

The research reported herein was in part supported by the New York Sea Grant Institute and by the Xerox Corporation through grants to Cornell University.

REFERENCES

1. P. L.-F. Liu and J. A. Liggett, 'Application of boundary element methods to problems of water waves', in P. K. Banerjee and R. P. Shaw (eds), *Developments in Boundary Element Methods—2*, Elsevier Applied Science, 1982, pp. 37–67.
2. J. A. Liggett and P. L.-F. Liu, 'Applications of boundary element methods to fluid mechanics', in C. A. Brebbia (ed), *Topics in Boundary Element Research*, Springer, 1984, pp. 78–96.
3. P. L.-F. Liu, 'Integral equation solutions to nonlinear free surface flows', *Proc. Finite Elements in Water Resources*, London, 1978, pp. 487–498.
4. M. S. Longuet-Higgins and E. D. Cokelet, 'The deformation of steep surface waves on water, I. A numerical method of computation' *Proc. R. Soc. Lond. A*, **350**, 1–26 (1976).
5. S. T. Grilli, J. Skourup and I. A. Svendsen, 'An efficient boundary element method for nonlinear water waves' *Eng. Anal. Boundary Elements*, **6**, 97–107 (1989).
6. T. Nakayama and K. Washizu, 'Boundary element method applied to analysis of two-dimensional nonlinear sloshing problems', *Int. j. numer. methods eng.*, **17**, 1631–1646 (1981).
7. N. Kamiya and H. Miyazawa, 'Sloshing in two-dimensional container with inclined side wall—boundary-element approach', *Commun. Appl. Numer. Methods*, **6**, 207–214 (1990).
8. S. K. Kim, P. L.-F. Liu and J. A. Liggett, 'Boundary integral equation solutions for solitary wave generation, propagation and run-up', *Coastal Eng.*, **7**, 299–317 (1983).
9. I. A. Svendsen and S. T. Grilli, 'Nonlinear waves on steep slopes' *J. Coastal Res.*, **7**, 185–202 (1989).
10. J. Skourup, 'A boundary integral equation model for the development of nonlinear water waves and their interaction with structures' *Series Paper No. 47*, Institute of Hydrodynamics and Hydraulics Engineering, Technical University of Denmark, 1989.
11. T. Vinje and P. Brevig, 'Numerical simulation of breaking waves', *Adv. Water Resources*, **4**, 77–82 (1981).
12. J. W. Dold and D. H. Peregrine, 'Steep unsteady water waves: an efficient computational scheme', *Proc. 19th Int. Conf. on Coastal Engineering*, Houston, TX, 1984, pp. 955–967.
13. S. N. Seo and R. A. Dalrymple, 'An efficient model for periodic overturning waves', *Eng. Anal. Boundary Elements*, **7**, 196–204 (1990).
14. W.-M. Lin, J. N. Newman and D. K. Yue, 'Nonlinear forced motions of floating bodies', *Proc. 15th Symp. on Naval Hydrodynamics*, Hamburg, 1984, pp. 33–47.
15. M. A. Grosenbaugh and R. W. Yeung, 'Nonlinear free-surface flow at a two-dimensional bow', *J. Fluid Mech.*, **209**, 57–75 (1989).
16. J. A. Liggett and P. L.-F. Liu, *The Boundary Integral Equation Method for Porous Media Flow*, George Allen and Unwin, London, 1983.
17. M. E. Mortenson, *Geometric Modeling*, Wiley, 1985.
18. R. G. Dean, 'Stream function representation of nonlinear ocean waves' *J. Geophys. Res.*, **70**, 4561–4572 (1965).
19. R. G. Dean, 'Evaluation and development of water wave theories for engineering application', *Vol. II, Special Rep. No. 1*, U.S. Army, Coastal Engineering Research Center, 1974.
20. G. Taylor, 'An experimental study of standing waves', *Proc. R. Soc. Lond. A*, **218**, 44–59 (1953).
21. W. G. Penney and A. T. Price 'Finite periodic stationary gravity waves in a perfect fluid', *Philos. Trans. R. Soc. Lond. A*, **244**, 254–284 (1952).
22. L. W. Schwartz and A. K. Whitney, 'A semi-analytic solution for nonlinear standing waves in deep water', *J. Fluid Mech.*, **107**, 147–171 (1981).